Chapter 2 | *Sample selection, observations and data reduction*

Abstract. In this Chapter I present accurate optical and near-infrared surface photometry of samples of edge-on disk galaxies, selected from both the northern and the southern hemispheres. The samples consist of highly inclined ($i \geq 87°$) disk galaxies with blue major axis diameters greater than 2.′2. The observed diameter-limited southern subsample is statistically complete ($V/V_{\rm max} = 0.502 \pm 0.253$) and can easily be corrected to represent a volume-limited sample.
The optical and near-infrared observations obtained in this thesis represent the largest sample of its kind for which high-quality and accurate surface photometry has been obtained to date. Our observations are both internally and externally consistent. The differences between observations obtained on different nights or with a different telescope and those between our luminosity profiles and those published previously are generally within the observational zero-point uncertainties.

1 The sample selection

1.1 Statistically complete samples

Spiral galaxies can, both physically and mathematically, very well be described by superimposing distinct components on top of each other, each with its own unique set of scale parameters.

If we want to compare the scale parameters obtained at different wavelengths, we need to make sure that the data are reduced and analysed in a consistent way. We also need a large, homogeneous data set, selected in such a way that unwanted selection biases are avoided. Only then we can draw conclusions based on statistical considerations rather than on individual cases.

Therefore, we need a large galaxy catalogue, from which we can select our sample. For northern-hemisphere galaxies we used the Uppsala General Catalogue of Galaxies (UGC; Nilson, 1973); we selected our southern sample from the Surface Photometry Catalogue of the ESO-Uppsala Galaxies (ESO-LV; Lauberts & Valentijn, 1989), because they contain large numbers of galaxies that were selected and parametrized in a uniform way.

To avoid inhomogeneities in the sample, we selected our samples based on the parameters available in these catalogues, although in some cases more accurate parameters are available in other catalogues or in the literature.

1.2 The ESO-LV sample

1.2.1 Selection criteria

The galaxies listed in the ESO-LV were taken from ESO sky survey plates that map the sky south of $\delta = -17.5°$, leaving out the area within 15° of the Galactic Equator, $|b| < 15°$, with the exception of a few fields with less than normal Galactic foreground extinction.

From these galaxies, we selected all candidates that met our selection criteria:

- the galaxy types range from S0 to Sd. Because we are interested in the structure parameters of disk galaxies, we selected all galaxies of revised Hubble type later than $T = -2$;
- they should be non-interacting and undisturbed;
- the angular blue diameters, D^B_{25}, are larger than 2.′2;
- their inclinations are greater than or equal to 87°.

1.2.2 From a volume-limited to a diameter-limited sample

For the study of undisturbed spiral and lenticular galaxies with clearly distinguishable disks presented in this thesis, we would ideally like to select a complete volume-limited sample. However, by defining a volume-limited sample based on a redshift limit, one would introduce incompleteness into the sample, due to the Malmquist bias. After all, it is likely that the smallest galaxies near the redshift limit are not catalogued, whereas the use of a lower redshift limit – in order not to miss any galaxies – will leave a small sample, which will contain very few large galaxies.

Another method to define a volume-limited sample is by taking galaxies belonging to one specific galaxy cluster. However, the possibility that a substantial part of these will be affected by gravitational interaction with neighbouring galaxies is significantly greater than that for non-cluster members. For that reason, this way of selecting galaxies is not well suited for the present study.

Therefore, we decided to select a diameter-limited sample, since this can be corrected easily to represent a volume-limited sample using a $V/V_{\rm max}$ test (e.g., Davies, 1990). The $V/V_{\rm max}$ test (Schmidt, 1968; Thuan & Seitzer, 1979) provides a handle on the degree of random distribution of the sampled objects in space. It has the nice property that we do not need to know the redshift of the galaxies involved. For a diameter-selected sample the ratio between the volume of the sphere determined by its distance (V), centred on the observer, and the maximum volume of the sphere in which the object could lie and still have been included in the catalogue ($V_{\rm max}$) is proportional to the ratio between the apparent angular diameter (D) and the minimum diameter of the sample selection criterion ($D_{\rm lim}$) in the following way:

$$\frac{V}{V_{\rm max}} = \left(\frac{\rm distance}{\rm distance_{max}}\right)^3 = \left(\frac{D_{\rm lim}}{D}\right)^3 \qquad (1)$$

For objects distributed randomly in space the average value of $V/V_{\rm max}$ equals $0.5 \pm 1/\sqrt{12 \times N}$, where N is the number of sample galaxies.

We selected all galaxies with either a blue angular diameter (at a surface brightness level of $\mu_B = 25$ mag arcsec^{-2}), D^B_{25}, or an original visual diameter, $D_{\rm vis}$, greater than 2.′2. In this way, we used a conservative diameter-selection criterion, since it has been shown that the $D_{\rm vis}$ is always greater than the real D^B_{25} (ESO-LV). In the ideal case we should have

selected galaxies based on their *red* angular diameters, in order to avoid unwanted effects due to dust contamination or to the influence of spiral arms. However, the ESO-LV does not contain these.

The ESO-LV is statistically complete down to blue angular diameters, D_{25}^B and $D_{\rm vis}$ combined, of $1.'0$ (Fig. 1). We need to be cautious when dealing statistically with galaxies larger than about $6'$, because there seem to be more galaxies with large apparent diameters than expected from a random space distribution above that limit. This might mean that apparently big galaxies are non-randomly distributed in space.

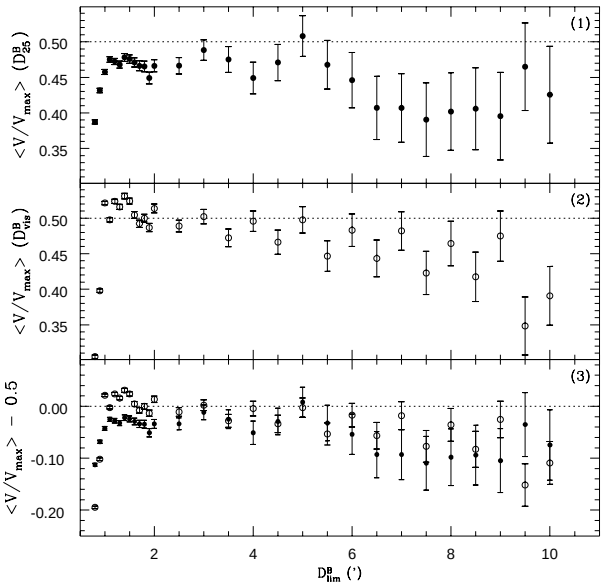

Fig. 1. $\langle V/V_{\rm max}\rangle$ values for the ESO-LV catalogue as a function of limiting blue diameter: (1) for D_{25}^B diameters; (2) for the original visual diameters; (3) degree of completeness for both methods. The dotted lines indicate the expected value of 0.5 for galaxies randomly distributed in space.

1.2.3 Inclination selection

Since we are interested in the vertical structures of spiral galaxies, unknown inclination effects should be avoided. Therefore, we defined our inclination lower limit to be $87°$. As van der Kruit & Searle (1981) showed, for systems having inclinations $i \geq 86°$ the slopes of both the radial and the vertical structures remain unaltered when increasing the inclination even further. However, in de Grijs et al. (1997, Chapter 8) we show that projection effects lead to an apparent thickening of the high-luminosity midplane of the galaxy. Deviations from an inclination of $90°$ cause a slight increase of the scale height, which becomes significant for inclinations smaller than $\sim 87 - 88°$.

Moreover, if we select galaxies that are highly inclined, we can very well study the effects of dust extinction on the galaxy luminosity distribution, without having to correct for inclination effects, for which the correction factors are yet unknown (see, e.g., Huizinga, 1994).

To select all objects of interest from the diameter-limited sample, we selected all galaxies with a (blue) axis ratio $(b/a)_{\rm org}$ of at least 3.1, which corresponds to a minimum inclination of $75°$ when assuming a conservative intrinsic axis ratio of $(b/a)_{\rm true} = 0.20$. In this way, highly inclined galaxies with prominent bulges will not be excluded from our final sample.

Finally, we examined those galaxies, for which the inclination angles obtained from the axis ratios were less than $87°$, by eye on the ESO sky survey plates. We selected only those galaxies that are really more than $87°$ inclined, which was done by examining the position of the dust lane – if present – across the galaxy, under the assumption that it follows the galaxy's symmetry plane. In general, we estimated the inclination based on the degree of symmetry of the galaxy light. Our final southern sample consisted of 93 edge-on galaxies. The characteristics of the subsample that we observed for this Ph.D. Thesis project are listed in Table 1.

To check the completeness of our southern sample we applied the $V/V_{\rm max}$ test to it. For this sample the mean $V/V_{\rm max}$ value results in 0.473 ± 0.181, so that we conclude that it is, within the errors, statistically complete. The final observed subsample is also statistically complete, with $V/V_{\rm max} = 0.502 \pm 0.253$.

1.3 The UGC sample

The UGC is based on the Palomar Sky Survey (POSS) plates, which cover the sky north of $\delta = -02°30'$. It is designed to be essentially complete to the limiting diameter of $1.'0$ on the blue prints. De Jong (1994) showed that the UGC is statistically complete down to red diameters of $1.'4$. Therefore, for the UGC we used a *red* major axis diameter selection criterion of $2'.0$. The red diameter was chosen so as to avoid possible dust and spiral arm effects, which are expected to show up most prominently in the young population's blue luminosity.

In order to be able to compare the results obtained for the UGC sample with those of the ESO-LV sample, similar selection criteria were applied to both catalogues.

After applying an inclination selection, whereby we only selected galaxies with UGC inclination class 7 (i.e., the most highly-inclined or "edge-on" objects), and after removing interacting or disturbed galaxies, we were left with 156 galaxies that met our selection criteria.

The final step was to examine the selected galaxies on the POSS plates in order to check their inclinations and, if necessary, to remove unsuitable galaxies from the sample. The resulting sample of selected objects consisted of 78 edge-on galaxies.

We also checked the completeness of the selected UGC sample and found a $\langle V/V_{\rm max}\rangle = 0.486 \pm 0.135$, which also indicates that we are dealing with a randomly distributed complete sample of (edge-on) galaxies.

The characteristics of the UGC subsample that was observed are described in more detail in de Grijs & van der Kruit (1996, Chapter 4).

The selection of the 9 galaxies observed out of our UGC sample and the 47 from the ESO-LV depended only on the observing time allocated by the SERC/PPARC (for the Royal Greenwich Observatory at La Palma, Spain) and ESO (for the European Southern Observatory at La Silla, Chile) time allocation panels, respectively. Under the assumption that our Galaxy is not located at an exceptional position in the Uni-

Table 1. Global parameters of the observed galaxies from our southern sample.
All parameters were taken from the ESO-LV, except the heliocentric velocities.
Columns: (1) and (2) Galaxy name (ESO-LV and alternative); (3) and (4) Center co-ordinates; (5) Revised Hubble type; (6) Blue major axis diameter at $\mu_B = 25$ mag arcsec^{-2}; (7) Axis ratio (originally estimated by eye in the ESO-LV); (8) and (9) Heliocentric velocity, corrected for Hubble flow, and corresponding reference. References: 1 – Da Costa et al. (1986); 2 – Da Costa et al. (1989); 3 – Knapp et al. (1989); 4 – Bottinelli et al. (1990); 5 – de Vaucouleurs et al. (1991) (RC3); 6 – Dressler (1991); 7 – Roberts et al. (1991); 8 – Mathewson et al. (1992); 9 – Schmidt & Boller (1992); 10 – Bottinelli et al. (1993); 11 – Schommer et al. (1993); 12 – Fisher et al. (1995)

Galaxy		RA	Dec	T	D_{25}^B	$(a/b)_{\rm org}$	v_0	velocity
ESO	Other	(1950.0)			(′)		(km/s)	reference
(1)	(2)	(3)	(4)	(5)	(6)	(7)	(8)	(9)
026-G06	IC 5026	20 41 55.0	−78 15 12.0	7.0	2.25	9.3	2323	8
033-G22		05 32 56.0	−73 47 00.0	7.0	2.20	12.5	3932	8
041-G09	IC 4484	14 42 45.0	−73 05 54.0	5.7	2.57	5.8	3559	8
074-G15	IC 5052	20 47 22.0	−69 23 30.0	7.0	7.12	5.4	426	9
138-G14		17 02 23.0	−62 01 00.0	6.5	4.98	8.0	3315	8
141-G27	IC 4819	19 02 43.0	−59 32 36.0	6.0	3.10	8.5	1452	8
142-G24	IC 4871/2	19 31 32.0	−57 37 48.0	6.7	3.95	8.4	2027	8
157-G18	IC 2058	04 16 50.0	−56 03 18.0	6.0	3.10	6.6	1342	8
201-G22		04 07 34.0	−48 51 24.0	5.0	2.52	7.3	4428	8
202-G35		04 30 55.1	−49 46 48.0	3.0	3.07	6.2	1527	8
235-G53		21 01 45.0	−47 59 18.0	3.0	2.55	6.0	5053	5
240-G11		23 35 08.0	−48 00 12.0	4.8	5.52	10.0	3390	8
263-G15		10 10 19.0	−47 02 48.0	6.0	3.10	8.0	2214	4
263-G18		10 11 25.0	−43 28 12.0	4.0	2.27	6.0	3902	[2]) 5
269-G15	NGC 4835A	12 54 23.0	−46 06 30.0	6.0	2.63	5.1	3355	8
286-G18		20 54 31.0	−43 34 00.0	4.0	2.70	6.4	9406	8
288-G25		21 56 11.0	−44 06 24.0	4.0	2.55	6.5	2453	2
311-G12		07 45 53.0	−41 19 36.0	0.0	4.18	6.4	848	10
315-G20		09 40 22.0	−41 35 12.0	10.0	2.4:	6.0	4543	12
321-G10		12 09 06.1	−38 16 12.0	0.0	2.12	7.3	2825	8
322-G73	NGC 4672	12 43 30.0	−41 26 00.0	−0.3	2.52	4.2	2966	11
322-G87	NGC 4696C	12 45 18.0	−27 18 18.0	3.0	2.00	5.0	2675	8
340-G08		20 13 49.0	−41 04 42.0	6.0	3.22	24.0	3004	8
340-G09		20 14 02.0	−38 49 48.0	7.0	2.67	9.0	2440	8
358-G26	IC 335/1963	03 33 34.0	−34 36 42.0	−2.0	2.55	4.5	1524	2
358-G29	NGC 1381	03 34 36.0	−35 27 30.0	−1.6	2.55	3.9	1657	2
377-G07		11 04 04.0	−36 25 30.0	6.0	2.0:	7.0	[1])	
383-G05		13 26 33.0	−34 00 54.0	3.7	3.18	6.3	3397	1
416-G25		02 46 34.2	−31 44 35.0	3.0	2.35	6.0	5720	8
435-G14		09 55 33.0	−28 16 00.0	5.0	2.70	7.3	3710	8
435-G25	IC 2531	09 57 41.0	−29 22 30.0	5.0	6.42	10.0	2384	8
435-G50		10 08 35.0	−30 10 36.0	6.0	2.38	21.0	2423	8
437-G62	NGC 3390	10 45 43.5	−31 16 10.0	3.0	3.07	4.5	2560	3,7
444-G21		13 20 43.1	−29 51 12.0	6.0	2.00	10.5	3844	8
446-G18		14 05 45.0	−29 20 00.0	3.0	2.52	9.7	4957	8
446-G44	IC 4393	14 14 53.0	−31 07 06.0	6.0	2.67	9.3	3240	8
460-G31		19 41 16.0	−27 31 36.0	4.5	2.58	9.5	5352	8
487-G02	NGC 1886	05 19 44.0	−23 51 36.0	3.5	3.33	7.5	2088	8
500-G24	NGC 3203	10 17 15.0	−26 26 48.0	−2.0	2.80	5.1	2142	3,7
505-G03		11 58 34.0	−24 17 30.0	7.0	2.73	5.6	1304	8
506-G02		12 17 34.0	−25 47 24.0	4.3	2.80	10.0	4950	8
509-G19		13 25 11.0	−25 35 48.0	4.0	2.77	11.3	10508	6
531-G22		21 37 36.0	−26 45 12.0	4.0	2.57	8.7	3639	8
555-G36		06 05 32.0	−19 54 24.0	5.0	2.33	11.5	[1])	
564-G27		09 09 37.0	−19 54 42.0	6.0	4.65	14.0	2897	8
575-G61		13 05 35.1	−20 44 06.0	7.0	2.05	14.0	1950	8
576-G33	NGC 5084	13 17 34.0	−21 33 54.0	3.0	10.88	6.8	1528	3,6,7

NOTES:
[1]) heliocentric velocity not available;
[2]) For ESO 263-G18 we used the heliocentric velocity of the nearby neighbour ESO 263-G19 as an approximation. Results obtained for this galaxy, involving distance-dependent parameters, should therefore be treated with caution.

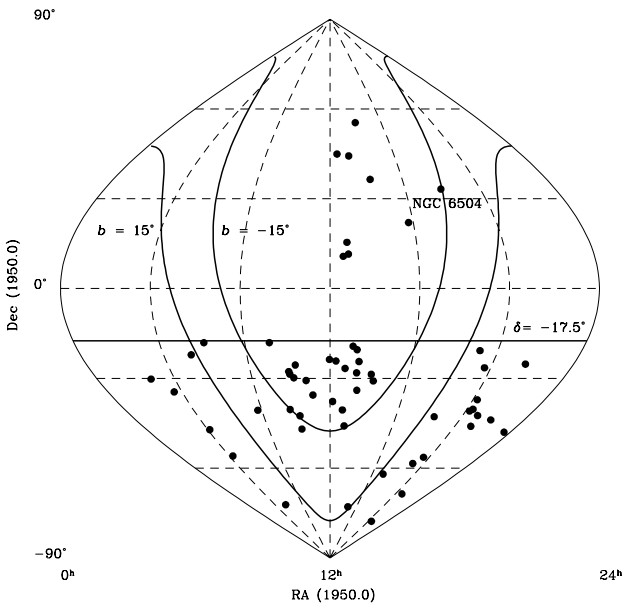

Fig. 2. Distribution on the sky of the observed sample galaxies. The thick drawn lines represent the selection boundaries, as described in the text.

verse, we are confident that our observations represent a statistically complete sample of edge-on disk galaxies. In Fig. 2 the distribution on the sky of the final observed sample is shown.

2 Observations

When observing highly inclined galaxies the effects of dust extinction start playing a major role in the visibility of the objects, depending on wavelength. To have a practically unobscured view of the galaxies we have observed the galaxies in the near-IR, where the obscuration by dust is much smaller than in the optical, although – in particular in the J band – not negligible.

To investigate the distribution of dust and stellar populations, we have also observed the galaxies in the optical passbands B, V, R, and I. From the resulting data set, one can easily obtain radial and vertical colour profiles, which are an important tool to study dust extinction and stellar population and metallicity gradients in galaxy disks (e.g., Chapter 5). The effect of dust extinction in edge-on galaxies is to redden the profiles, although a complicating factor is the radial change of stellar population colours. We expect to find redder colours in the galaxy centres due to the redder (and older) stellar populations (and higher metallicities) in the bulge than in the disk, and also because of the increasingly important extinction effects towards both the galaxy centres and the midplanes.

In the following we will describe the observations and observing techniques used for the near-infrared and the optical passbands separately.

2.1 The Near-Infrared Observations

Of the total sample of 93 southern edge-ons, 27 were observed in the near-infrared in two observing runs of 4 and 3 nights, respectively, with the IRAC2B camera at the ESO/MPI 2.2m telescope of the European Southern Observatory at La Silla, Chile. The IRAC2B camera is equipped with a Rockwell 256×256 pixel NICMOS3 HgCdTe array for imaging through broad and narrow band filters between 1 and 2.5 μm. For both observing runs, in July 1994 and January 1995, we used the IRAC2B camera with Objective C, corresponding to a pixel size of $0.''491$ (40 μm) and a field of view of $125'' \times 125''$. This mode is recommended for broad-band observations, when background noise dominates, since it has the highest efficiency, yields the maximum square field and provides reasonable sampling under average seeing conditions.

At our July 1994 observing run we took a series of (flat-field) exposures with different integration times in order to check its linearity. In Fig. 3 we show that the near-infrared array is linear to within 1% up to $\sim$ 18,000 counts (which is more than the maximum flux obtained for our objects) for exposure times $>$ 1 sec. In this figure the dotted line represents mean count rates derived from the entire frames, whereas the short-dashed line was obtained from measurements in a smaller region in which the intensity peaks in all frames that were used for the linearity check. As a comparison, we also plotted the results obtained for an "average" region (sized about half the total array size) (long-dashed line). If we look at the lower three panels of Fig. 3, it appears that the errors between the different regions considered are correlated. This does not influence the degree of linearity, however.

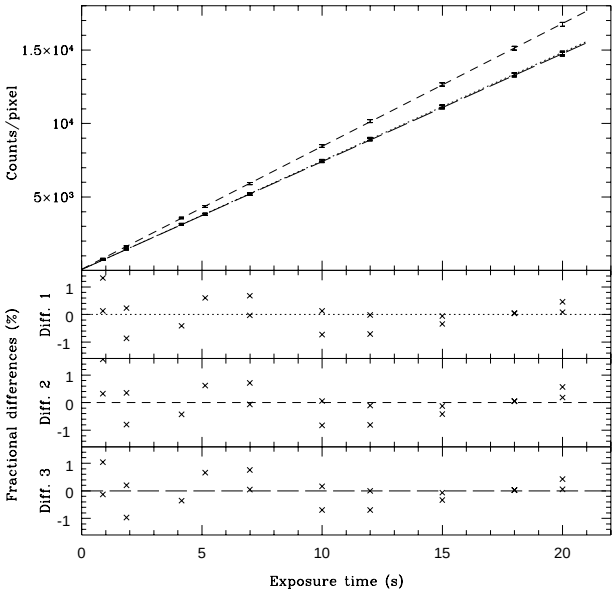

Fig. 3. Linearity test of the NICMOS3 near-infrared array. The lower three panels display the differences between the best-fitting lines in the top panel and the data for (1) the entire array; (2) the highest-intensity region; and (3) an "average" part of the array.

At both runs we used the standard Johnson J and the K' filters (Wainscoat & Cowie, 1992), while for the July 1994 observations of ESO 446-G18 we also observed in the John-

son H band. We chose to observe in K' (central wavelength $\lambda_c = 2.15\mu$m, bandwidth $\Delta\lambda = 0.32\mu$m) rather than in the K band ($\lambda_c = 2.2\mu$m, $\Delta\lambda = 0.4\mu$m), since K' is almost as little affected by dust as the K band, but has a lower sky background. The quality of the K'-band observations of ESO 138-G14 was too poor to be used.

The NICMOS3 array contains of order 0.5% bad pixels; on one side the edge of the array is unreliable due to intrinsic quantum efficiency variations with time. We avoided this region in the data reduction, because the data in this region cannot be flatfielded accurately.

A complicating factor when dealing with near-infrared observations is the fact that the sky fluctuates rapidly, and it also is about 10^4 times brighter than the faint outer regions of the galaxies. Therefore, in the near-infrared it is advisable to observe as many sky images as object frames, so that accurate flatfielding and sky subtraction can be done. We took sky images and object frames alternately, with equal integration times, and spatially separated by $\sim 5'$. Because of the high sky background in the near-infrared passbands saturation of the array elements will occur already with short exposure times. Therefore, our near-infrared observations were done by taking several short exposures at the same position. These were averaged on-line at the telescope. For our J-band observations we used exposure times of 4×30s and in H and K' we took exposure sequences of 12×10s.

An overview of all near-infrared observations can be found in Table 2.

2.2 The Optical Observations

2.2.1 The ESO-LV data

The optical observations of our southern sample were obtained at both the Danish 1.54m and the Dutch 0.92m telescopes of the European Southern Observatory at La Silla, Chile. Both telescopes were used in direct imaging mode, at prime focus.

The major part of the observations were obtained using the Danish 1.54m telescope, equipped with a 1081×1040 pixel TEK CCD with a pixel size of 24μm (0.36″/pix). It was used in slow read-out mode to decrease the pixel-to-pixel noise. During two observing runs, in January and July 1994, respectively, 31 edge-on galaxies were mapped, roughly covering the entire southern sky. The CCD used is linear to within 1% up to 44,000 counts and saturates at 65,536 counts.

Gaps in the observed sample were filled in by service observations with the Dutch 0.92m telescope, equipped with a 512×512 pixel TEK CCD. It has a pixel size of 27 μm (0.44″/pix), giving a field of view of $3.'9 \times 3.'9$. The CCD is linear to within 1% over the full 16-bit dynamic range. Service observations in Dutch time were obtained in April 1993, December 1993, January and October 1994, January 1995, and March 1996.

At both telescopes we used the standard Johnson B and V filters and the Thuan & Gunn (1976) i filter, which characteristics match those of a Johnson I filter (Buser, 1978). At the Dutch telescope observations were also obtained with a standard Johnson R filter (see, e.g., Bessel, 1990).

The complete observing log of the optical observations can be found in Table 3.

Table 2. Log of the near-infrared observations
Columns: (1) Galaxy name (ESO-LV); (2) Date of observation (ddmmyy) (3) Passband; (4) Exposure time (sec); (5) Seeing FWHM (″)

Galaxy (1)	Date (2)	Band (3)	Exp.time (4)	Seeing (5)
026-G06	110794	J	2×4×30	1.6
	110794	K'	2×12×10	1.5
041-G09	100794	J	2×4×30	1.9
	090794	K'	3×12×10	1.5
074-G15	110794	K'	2×12×10	1.5
138-G14	100794	J	2×4×30	1.4
	090794	K'	2×12×10	1.3
141-G27	100794	J	2×4×30	1.5
	090794	K'	2×12×10	1.4
142-G24	100794	J	2×4×30	1.6
	090794	K'	2×12×10	1.4
157-G18	250295	J	2×4×30	1.5
	240295	K'	2×12×10	1.1
201-G22	250295	J	2×4×30	1.4
	240295	K'	2×12×10	1.1
263-G15	250295	J	2×4×30	1.5
	240295	K'	12×10	1.4
	250295	K'	12×10	1.4
286-G18	100794	J	1.5×4×30	1.7
	110794	J	4×30	1.5
	090794	K'	12×10	1.6
	110794	K'	12×10	1.2
311-G12	250295	J	2×4×30	1.4
	240295	K'	2×12×10	0.9
315-G20	250295	J	2×4×30	1.1
	240295	K'	2×12×10	1.1
340-G09	100794	J	2×4×30	1.9
	090794	K'	2×12×10	1.5
358-G29	260295	J	4×30	1.5
	260295	K'	2×12×10	1.5
383-G05	100794	J	2×4×30	1.2
	090794	K'	2×12×10	1.1
416-G25	260295	J	2×4×30	1.5
	260295	K'	2×12×10	1.4
435-G14	250295	J	2×4×30	1.2
	240295	K'	2×12×10	1.5
435-G25	250295	J	2×12×10	1.1
	240295	K'	2×12×10	1.6
437-G62	260295	J	3×4×30	1.2
	260295	K'	2×12×10	1.1
446-G18	100794	J	2×4×30	1.4
	120794	H	12×10	1.0
	090794	K'	2×12×10	1.3
	120794	K'	2×12×10	1.0
446-G44	100794	J	4×30	2.1
	090794	K'	2×12×10	1.4
460-G31	110794	J	2×4×30	1.5
	090794	K'	2×12×10	1.5
487-G02	250295	J	2×4×30	1.6
	240295	K'	2×12×10	1.1
500-G24	260295	J	2×4×30	1.2
	250295	K'	2×4×30	1.6
509-G19	100794	J	2×4×30	1.3
	100794	K'	2×12×10	1.2

Table 2. (Continued)

Galaxy (1)	Date (2)	Band (3)	Exp.time (4)	Seeing (5)
564-G27	250295	J	2×4×30	1.1
	240295	K'	2×12×10	0.9
576-G33	110794	J	2×12×10	1.2
	110794	K'	2×4×30	1.0

2.2.2 The UGC data

Imaging CCD observations of 8 edge-on galaxies in B, V, R, and I were obtained with the 1m Jacobus Kapteyn Telescope (JKT) of the Observatorio del Roque de los Muchachos at La Palma (Spain), equipped with the EEV7 P88300 CCD. This CCD, with 1280×1180 pixels and a pixel size of 0.″30, was used in slow read-out mode, in this way reducing the read-out noise to below the sky noise. Its response is linear to within 1%, both in slow and in quick read-out mode. We used the B, V and R Harris filters and the Kitt Peak I filter available on La Palma (RGO/La Palma Technical Notes, 1987; 1990).

These observations will be discussed in more detail in Chapters 3 and 4.

2.3 Image processing and data reduction

In the following I will describe the techniques used for the reduction and image processing of the optical and near-infrared observations. Since the first steps of the reduction process differ substantially, they will be treated separately until the calibration phase of the individual images is reached. The calibration and extraction of the parameters is essentially the same for both the optical and the near-infrared images and will therefore be dealt with together.

2.3.1 Reduction of the Near-Infrared Images

Because of the dominant sky contribution in the near-infrared, great care has to be taken when reducing near-infrared observations, especially when flatfielding, sky subtracting and mosaicing.

Since it is impossible to determine the dark current of the IRAC2B (NICMOS3) array during an exposure, dark frames are not very useful. An additional problem has to be dealt with regarding the dark current: its amplitude depends on the amount of light that falls onto the array. Therefore, the dark current is higher in the K' band than in J, where the background sky level is lower.

In order not to be hindered by dark current effects we took a number of dome flat fields with a lamp on and a number with the lamp switched off. From these, an average (median-filtered) flat field was constructed in all passbands concerned; the effect of the dark current was taken out by combining the two sets of flatfields.

Similarly, because we observed as many sky images as images of the objects themselves, of equal exposure times, when subtracting sky frames from the object frames, also here the dark current was cancelled out. Each sky frame was compared with the two sky frames taken nearest in time in order to detect stars in the sky frames. These stars were filtered out using

Table 3. Optical observations of the southern sample. Columns: (1) Galaxy name (ESO-LV); (2) Telescope used (Dan 1.5 = Danish 1.54m; Dut 0.9 = Dutch 0.92m); (3) Date of observation (ddmmyy) (4) Passband; (5) Exposure time (sec); (6) Seeing FWHM (″).

Galaxy (1)	Tel. (2)	Date (3)	Band (4)	Exp.time (5)	Seeing (6)
026-G06	Dan 1.5	090794	B	2×1800	2.1
	Dan 1.5	090794	V	2100	2.0
	Dan 1.5	090794	I	2×900	1.6
033-G22	Dan 1.5	120194	B	2×1500	1.7
	Dan 1.5	120194	V	2100	1.6
	Dan 1.5	120194	I	2×900	0.9
041-G09	Dan 1.5	100794	B	2×1800	1.7
	Dan 1.5	100794	V	2100	1.6
	Dut 0.9	060493	R	720	1.7
	Dan 1.5	100794	I	2×900	1.4
074-G15	Dan 1.5	110794	B	2×1800	1.5
	Dan 1.5	110794	V	2100	1.3
	Dan 1.5	110794	I	2×900	1.3
138-G14	Dan 1.5	080794	B	2×1800	2.2
	Dan 1.5	080794	V	2100	1.9
	Dan 1.5	080794	I	2×900	1.6
141-G27	Dan 1.5	090794	B	2×1800	1.4
	Dan 1.5	090794	V	2100	1.7
	Dut 0.9	260493	R	600	1.6
	Dan 1.5	090794	I	2×900	1.2
142-G24	Dan 1.5	110794	B	2×1800	1.2
	Dan 1.5	110794	V	2100	1.6
	Dan 1.5	110794	I	2×900	1.4
157-G18	Dan 1.5	100194	B	2×1500	1.1
	Dan 1.5	100194	V	2×900	1.2
	Dan 1.5	100194	I	2×900	1.2
201-G22	Dan 1.5	090194	B	2×1500	1.3
	Dan 1.5	090194	V	2100	1.1
	Dan 1.5	090194	I	2×900	1.2
202-G35	Dut 0.9	051094	B	2×1800	1.4
	Dut 0.9	051094	V	2×900	1.2
	Dut 0.9	061094	I	2×900	1.2
235-G53	Dan 1.5	110794	B	2×1800	1.4
	Dut 0.9	270994	V	2×1200	1.7
	Dan 1.5	120794	I	600	1.5
	Dut 0.9	170396	I	1200	1.3
	Dut 0.9	210396	I	1200	1.3
240-G11	Dut 0.9	051094	B	2×1800	1.6
	Dut 0.9	061094	B	2×1800	1.6
	Dut 0.9	051094	V	2×1200	1.6
	Dut 0.9	061094	V	2×1200	1.6
	Dut 0.9	051094	I	2×1200	1.6
	Dut 0.9	061094	I	2×1200	1.6
263-G15	Dan 1.5	120194	B	2400	1.1
	Dan 1.5	120194	V	2×900	1.0
	Dan 1.5	090194	I	900	1.0
	Dan 1.5	100194	I	600	1.1
	Dan 1.5	120194	I	900	1.0
263-G18	Dut 0.9	100493	B	2400	1.7
	Dut 0.9	200194	V	3×900	1.2
	Dut 0.9	110493	R	720	1.3
	Dut 0.9	190194	I	2×900	1.2
269-G15	Dut 0.9	130493	B	2400	2.1
	Dut 0.9	130396	V	2400	1.4
	Dut 0.9	130493	R	720	1.9

Table 3. (Continued)

Galaxy (1)	Tel. (2)	Date (3)	Band (4)	Exp.time (5)	Seeing (6)
	Dut 0.9	130396	*I*	2×1200	1.3
286-G18	Dan 1.5	110794	*B*	2×1200	1.3
	Dan 1.5	090794	*V*	2100	1.6
	Dan 1.5	090794	*I*	2×900	1.3
288-G25	Dut 0.9	051094	*B*	2×1800	1.3
	Dut 0.9	051094	*V*	2×1200	1.3
	Dut 0.9	051094	*I*	2×1200	1.3
311-G12	Dan 1.5	120194	*B*	2×1500	1.0
	Dan 1.5	120194	*V*	2100	1.0
	Dan 1.5	120194	*I*	2×900	1.0
315-G20	Dan 1.5	090194	*B*	2×1500	1.4
	Dut 0.9	060194	*V*	3300	1.1
	Dan 1.5	090194	*V*	900	1.2
	Dut 0.9	120493	*R*	720	1.6
	Dan 1.5	090194	*I*	2×900	1.7
321-G10	Dut 0.9	280493	*B*	2400	1.3
	Dut 0.9	280493	*R*	720	1.2
	Dut 0.9	280493	*I*	300	1.2
322-G73	Dut 0.9	270493	*B*	2400	1.6
	Dut 0.9	230396	*V*	2400	1.7
	Dut 0.9	270493	*R*	720	1.4
	Dut 0.9	230396	*I*	2×1200	1.2
322-G87	Dut 0.9	270493	*B*	2400	1.6
	Dut 0.9	270493	*R*	720	1.3
	Dut 0.9	270493	*I*	300	1.3
340-G08	Dan 1.5	100794	*B*	2×1800	1.6
	Dan 1.5	100794	*V*	2100	1.3
	Dan 1.5	100794	*I*	2×900	1.3
340-G09	Dan 1.5	100794	*B*	2×1800	2.0
	Dan 1.5	100794	*V*	300	1.2
	Dan 1.5	110794	*V*	1500	1.2
	Dut 0.9	140396	*I*	2×1200	1.4
358-G26	Dan 1.5	120194	*B*	2×1500	1.0
	Dan 1.5	120194	*V*	2100	1.1
	Dan 1.5	120194	*I*	1200	1.0
358-G29	Dan 1.5	100194	*B*	2×1500	1.0
	Dan 1.5	100194	*V*	2100	1.1
	Dan 1.5	100194	*I*	2×900	1.3
377-G07	Dut 0.9	120493	*B*	2400	2.2
	Dut 0.9	100396	*V*	2400	1.4
	Dut 0.9	120493	*R*	720	2.1
	Dut 0.9	100396	*I*	2×1200	1.2
383-G05	Dan 1.5	080794	*B*	2×1800	2.0
	Dan 1.5	080794	*V*	2100	1.4
	Dan 1.5	080794	*I*	2×900	1.3
416-G25	Dan 1.5	130194	*B*	2×1500	1.2
	Dan 1.5	130194	*V*	2×900	1.0
	Dan 1.5	130194	*I*	2×900	1.0
435-G14	Dut 0.9	080493	*B*	2400	1.6
	Dut 0.9	201293	*B*	1000	1.7
	Dut 0.9	201293	*V*	2×900	1.3
	Dut 0.9	080493	*R*	720	1.2
	Dut 0.9	201293	*I*	2×900	1.0
435-G25	Dut 0.9	230493	*B*	5400	1.9
	Dut 0.9	231293	*B*	1800	1.8
	Dut 0.9	311293	*B*	1800	1.4
	Dut 0.9	050194	*B*	1800	1.5
	Dut 0.9	060194	*B*	1800	1.3
	Dut 0.9	221293	*V*	3300	1.2

Table 3. (Continued)

Galaxy (1)	Tel. (2)	Date (3)	Band (4)	Exp.time (5)	Seeing (6)
	Dut 0.9	231293	*V*	3000	2.1
	Dut 0.9	060194	*V*	2×900	1.1
	Dut 0.9	230493	*R*	2×720	1.6
	Dut 0.9	230493	*I*	2×300	1.7
	Dut 0.9	231293	*I*	2×900	1.3
	Dut 0.9	060194	*I*	2×900	1.2
435-G50	Dan 1.5	100194	*B*	2×1500	1.2
	Dan 1.5	100194	*V*	2100	1.0
	Dan 1.5	100194	*I*	2×900	1.1
437-G62	Dut 0.9	040195	*B*	2×1800	1.3
	Dut 0.9	040195	*V*	2×1200	1.5
	Dut 0.9	040195	*I*	2×1200	1.0
444-G21	Dut 0.9	180493	*B*	2400	1.6
	Dut 0.9	230396	*V*	2400	1.3
	Dut 0.9	180493	*R*	720	1.2
	Dut 0.9	230396	*I*	2×1200	1.2
446-G18	Dan 1.5	090794	*B*	2×1800	1.2
	Dan 1.5	090794	*V*	2100	1.3
	Dut 0.9	130493	*R*	720	1.8
	Dan 1.5	090794	*I*	2×900	1.1
446-G44	Dan 1.5	110794	*B*	2×1800	1.1
	Dan 1.5	110794	*V*	2100	1.1
	Dut 0.9	230493	*R*	720	1.2
	Dut 0.9	140396	*I*	2×1200	1.2
460-G31	Dan 1.5	080794	*B*	900	1.2
	Dan 1.5	100794	*B*	2700	1.3
	Dan 1.5	080794	*V*	2100	1.8
	Dan 1.5	080794	*I*	2×900	1.5
487-G02	Dan 1.5	090194	*B*	2×1500	1.3
	Dan 1.5	090194	*V*	2100	1.2
	Dan 1.5	090194	*I*	2×900	1.1
500-G24	Dan 1.5	130194	*B*	2×1500	1.2
	Dan 1.5	130194	*V*	2×900	1.1
	Dan 1.5	130194	*I*	2×900	1.0
505-G03	Dut 0.9	280493	*B*	2400	1.3
	Dut 0.9	010496	*V*	2400	1.4
	Dut 0.9	280493	*R*	720	1.2
	Dut 0.9	010496	*I*	2×1200	1.3
506-G02	Dut 0.9	280493	*B*	2400	1.2
	Dut 0.9	280493	*R*	720	1.1
	Dut 0.9	280493	*I*	300	1.0
509-G19	Dan 1.5	100794	*B*	2×1800	1.3
	Dan 1.5	100794	*V*	2100	1.2
	Dut 0.9	180493	*R*	720	1.3
	Dan 1.5	100794	*I*	2×900	1.0
531-G22	Dut 0.9	270994	*B*	2×1800	1.6
	Dut 0.9	270994	*V*	2×1200	1.5
	Dut 0.9	270994	*I*	2×1200	1.5
555-G36	Dan 1.5	130194	*B*	2×1500	1.2
	Dan 1.5	130194	*V*	2×900	1.1
	Dan 1.5	130194	*I*	2×900	1.1
564-G27	Dut 0.9	211293	*B*	2400	1.4
	Dut 0.9	221293	*B*	1800	1.7
	Dut 0.9	211293	*V*	4500	1.4
	Dut 0.9	221293	*V*	3000	1.8
	Dut 0.9	211293	*I*	2×900	1.4
	Dut 0.9	221293	*I*	2×900	1.3

Table 3. (Continued)

Galaxy	Tel.	Date	Band	Exp.time	Seeing
(1)	(2)	(3)	(4)	(5)	(6)
575-G61	Dut 0.9	260493	B	1800	1.6
	Dut 0.9	230396	V	2400	1.3
	Dut 0.9	260493	R	720	1.3
	Dut 0.9	230396	I	2×1200	1.2
576-G33	Dut 0.9	180493	B	2400	1.0
	Dan 1.5	120794	B	2×1800	1.2
	Dan 1.5	120794	V	2100	1.0
	Dut 0.9	180493	R	720	1.1
	Dut 0.9	180493	I	300	1.1
	Dan 1.5	120794	I	2×900	1.2

a median filter and thus the resulting cleaned sky images truly represented the actual sky contributions.

Once the individual object frames had been reduced, we combined them into mosaics, because usually the galaxy sizes were much larger than the field of view of the near-infrared array. For most galaxies, either 4 or 8 individual frames were used for the mosaicing. Moreover, to get rid of the effects of bad pixels and to obtain accurate flatfielding we moved the object across the array between subsequent exposures, so that mosaicing of the image frames was required to obtain complete galaxy images. The mosaicing was done using common stars in the frames for the determination of the exact spatial offsets. In the rare case that no common stars could be determined, we used the telescope offsets as our mosaicing offsets. The overlapping area was used to determine the adjustment of sky levels needed, by means of a least squares fit, both when mosaicing two and more than two images together. The limiting factors here were flatfielding errors.

Bad pixels and areas on the array were masked out and not considered during the entire reduction process. Only after mosaicing was finished, the areas that were masked out were interpolated and given the median value of the surrounding pixels (see also Peletier [1993] for a detailed description of the reduction method used).

2.3.2 Reduction of the Optical Images

The standard photometric reduction was applied to the CCD images by using the Iraf data reduction package, developed by the National Optical Astronomical Observatories.

Bias subtraction was done using the average value of the overscan region on the CCD. A number of bias frames was obtained at the beginning and end of each night. These were checked for constancy of the mean bias level during each night and the existence of possible underlying structures. The bias level proved to be constant within 1% during each night, whereas no obvious structures were found in the bias frames.

To reduce the influence of detector noise, we combined twilight flat fields from several nights to create a very accurate flat field for each passband. The variations in flat field structures from night to night were less than 0.5% of the total intensity of the individual flat fields, although on small scales the variations could exceed the 3% level due to dust patches on the CCD window. However, since we are interested in large-scale structures, these local variations do not affect our results significantly other than that they make the calibration slightly more cumbersome.

Possible gradients in the background, mainly due to moon light, were removed by a background fitting routine, which fitted a two-dimensional polynomial (linear in both dimensions, tilted plane) to regions far away from the galaxy and subtracted this two-dimensional plane from the image; the remaining background variations are statistical: the uncertainties are mainly due to Poisson noise.

Cosmic ray events were removed when stacking frames obtained with the same filters. The cosmic ray removal routine checked for pixels above the expected noise with a point spread function smaller than the estimated seeing. In case of a cosmic ray detection, the affected pixel was replaced by the median value of the surrounding pixels. The routine was applied with a conservative selection limit, so as not to remove real structures from the science frames.

Special care was taken to stack frames with the same resolution. In some cases the frames taken under the best seeing conditions had to be degraded slightly. In a few cases, if the galaxy sizes exceeded the sizes of the CCDs, the individual frames were mosaiced to form complete images of the galaxies. The mosaicing procedure was described in Sect. 2.3.1.

For some of the observed sample galaxies the seeing is rather bad (i.e., larger than $2''$). However, this does not influence the results presented in this Ph.D. Thesis significantly, because the structures looked at extend over many seeing cells and thus the slopes of the surface brightness profiles are not affected significantly. The models used take into account the seeing of the images, so that a seeing deconvolution can be applied to the extracted profiles.

2.3.3 Calibration of the Observations

During all observing runs, we observed a number of fields with standard stars, to be used for the calibration of our images. For the optical observations Landolt fields were used (Landolt, 1992a), as well as some secondary standard stars from Stone & Baldwin (1983), for which the broad-band photometry was provided by Landolt (1992b). In this way we calibrated our observations to Johnson B, and V, and Kron-Cousins R and I.

The calibration of the near-infrared observations was done by using the SAAO/ESO/ISO Faint Standard Stars (Carter & Meadows, 1995). We used the corrections published by Wainscoat & Cowie (1992) to transform the K' measurements to the K band.

Standard stars and fields were taken at least three times a night at different airmasses during all observing runs. This provided us with the possibility to determine the atmospheric extinction during the photometric nights, as well as during all observing runs.

Instrumental magnitudes of all standard stars observed were determined. All magnitudes of one observing run were combined, after eliminating data from non-photometric (parts of) nights. Next, zero-point magnitudes, extinction and colour corrections were calculated in the following way:

$$
\begin{aligned}
b &= B + c_{0,B} + c_{1,B}(B-V) + c_{2,B}X \\
v &= V + c_{0,V} + c_{1,V}(B-V) + c_{2,V}X \\
r &= R + c_{0,R} + c_{1,R}(V-R) + c_{2,R}X \\
i &= I + c_{0,I} + c_{1,I}(V-I) + c_{2,I}X \\
& \qquad\qquad (2) \\
j &= J + c_{0,J} + c_{2,J}X \\
h &= H + c_{0,H} + c_{2,H}X \\
k &= K + c_{0,K} + c_{2,K}X
\end{aligned}
$$

where B, V, R, I, J, H, and K are the standard magnitudes, b, v, r, i, j, h, and k the instrumental magnitudes per second, X the airmass during the observation, and $c_{i,<\mathrm{band}>}$ $(i = 0, 1, 2)$ the transformation coefficients to be determined. For the near-infrared observations colour coefficients could not be determined accurately due to the fewer data points available. The transformation coefficients we obtained are listed in Table 4. In general, as can be seen by looking at the variation in and the estimated errors of the zero-point offsets, the data acquired at the Danish 1.54m telescope is of better quality than that obtained with the Dutch 0.92m telescope.

Galaxy observations taken at non-photometric (parts of) nights were calibrated by using observations taken at photometric (parts of) nights, if available. This was only done if the non-photometric images could be flatfielded to approximately the same level of accuracy as the corresponding photometric observations, so that deeper light levels could be reached.

Finally, the pixel sizes of the different CCDs used were determined, as well as the orientation of the CCDs. Landolt standard fields (Landolt, 1992a) were used to do so; the resulting parameters are tabulated in Table 5. We found that during none of the observing runs the CCD orientation was exactly North-South, the mismatches are also tabulated in Table 5.

2.3.4 Profile Extraction

To study galaxy properties statistically, we have to extract the parameters in a consistent way. Therefore, we developed a program to extract luminosity profiles from the reduced optical and near-infrared observations.

First, we aligned the observations taken through the different filters, using common (foreground) stars in the individual frames. Only in those cases where foreground stars were completely lacking the galaxy centres were used for the alignment. One has to be cautious in doing so, as the galaxy morphology might be different in the different passbands because of dust obscuration and population changes.

In order not to be hindered by contamination of the galaxy luminosity by foreground star light, we used the I-band images to mask out those areas contaminated by foreground stars. We used the mask thus obtained to correct for foreground star contamination in the other passbands as well.

We extracted luminosity profiles at a number of positions along both the major and the minor axes of the sample galaxies. To do so, the galaxies were binned semi-logarithmically both radially and vertically to retain an approximately constant overall signal-to-noise ratio in the resulting vertical profiles and to be able to follow the profiles further out.

In the analysis of the individual profiles, we distinguish between the different sides of the major and minor axis, respectively, to avoid possible dust contamination in the case

Table 4. Calibration transformation coefficients obtained for the different observing runs.

Passband (1)	zero point offset (c_0) [1] (2)	colour coeff. (c_1) (3)	extinction (mag/airmass) (c_2) (4)
April 1993, Dutch 0.9m telescope			
B	20.721 ± 0.109	0.110 ± 0.032	0.221 ± 0.030
R	21.473 ± 0.077	0.063 ± 0.025	0.126 ± 0.022
I	20.606 ± 0.083	−0.037 ± 0.015	0.097 ± 0.030
December 1993/January 1994, Dutch 0.9m telescope			
B	20.982 ± 0.087	0.111 ± 0.027	0.242 ± 0.045
V	21.679 ± 0.043	0.034 ± 0.012	0.129 ± 0.033
I	20.853 ± 0.048	−0.036 ± 0.013	0.104 ± 0.029
January 9–13, 1994, Danish 1.54m telescope			
B	22.331 ± 0.040	0.124 ± 0.031	0.105 ± 0.030
V	23.058 ± 0.038	0.039 ± 0.033	0.054 ± 0.033
I	22.351 ± 0.040	−0.035 ± 0.022	0.021 ± 0.013
July 9–13, 1994, Danish 1.54m telescope			
B	22.984 ± 0.056	0.157 ± 0.006	0.308 ± 0.051
V	23.511 ± 0.024	0.038 ± 0.016	0.128 ± 0.044
I	22.497 ± 0.028	−0.042 ± 0.018	0.030 ± 0.022
September/October 1994, Dutch 0.9m telescope			
B	21.232 ± 0.059	0.058 ± 0.027	0.210 ± 0.042
V	21.758 ± 0.054	−0.004 ± 0.022	0.153 ± 0.036
R	21.901 ± 0.022 [2]	[2]	0.126 ± 0.032
I	20.972 ± 0.048	−0.060 ± 0.018	0.064 ± 0.023
January 1995, Dutch 0.9m telescope			
B	20.900 ± 0.043	0.144 ± 0.030	0.242 ± 0.449
V	21.643 ± 0.023	0.055 ± 0.024	0.128 ± 0.033
I	20.896 ± 0.017	−0.025 ± 0.015	0.065 ± 0.023
March 1996, Dutch 0.9m telescope			
V	21.875 ± 0.040	0.039 ± 0.021	0.126 ± 0.037
I	20.928 ± 0.031	−0.037 ± 0.018	0.093 ± 0.032
July 9–12, 1994, ESO 2.2m telescope			
J	21.284 ± 0.074		0.193 ± 0.052
H	21.221 ± 0.055		0.1 (assumed) [3]
K	20.772 ± 0.088		0.002 ± 0.035
February 24–26, 1995, ESO 2.2m telescope			
J	21.574 ± 0.078		0.114 ± 0.048
K	20.697 ± 0.080		0.003 ± 0.029

NOTES:

[1]) Although the errors in the zero-point offsets quoted may be considerable, the errors obtained on the individual nights were significantly smaller. Therefore, the latter were used for the data reduction.

[2]) For the September/October 1994 observing run too few data points were available to estimate this colour coefficient accurately. The R band zero-point offset was not corrected for possible colour mismatches.

[3]) Due to the small number of H band observations and the small range of airmasses, the extinction coefficient could not be determined unambiguously. Therefore, an assumed value of 0.1 mag/airmass was used.

Table 5. Characteristics of the different CCDs used for our observations

Observing dates	Telescope	Pixel size ($''$)	Misalignment N-S ($^\circ$)
(1)	(2)	(3)	(4)
April 1993	Dut 0.9	0.397 ± 0.052	2.88 ± 2.89
Dec. 1993/Jan. 1994	Dut 0.9	0.434 ± 0.044	2.68 ± 1.62
Sept./Oct. 1994	Dut 0.9	0.442 ± 0.042	2.72 ± 1.83
January 1995	Dut 0.9	0.444 ± 0.045	-0.51 ± 1.28
March 1996	Dut 0.9	0.443 ± 0.023	1.46 ± 0.92
January 9–13, 1994	Dan 1.5	0.359 ± 0.016	0.28 ± 0.04
July 9–13, 1994	Dan 1.5	0.359 ± 0.023	0.17 ± 0.42
July 9–12, 1994	ESO 2.2	0.491 ± 0.008	0.11 ± 0.10
February 24–26, 1995	ESO 2.2	0.491 ± 0.012	0.06 ± 0.13

of not perfectly edge-on orientations and the effects of stellar warps and patchy spiral arms.

The positions of the galaxy centres were determined by folding the profiles and under the assumption of symmetrical light distributions (in the case of perfectly edge-on orientations) with respect to the galaxy planes.

3 Internal and external consistency checks

3.1 Internal consistency checks

To get an impression of the quality of our observations, we performed both internal and external consistency checks. We observed some of our sample galaxies more than once through the same filter either with the same telescope but on different nights, or with a different telescope during an other observing run. These observations provide us with an internal consistency check. Fig. 4 shows the difference between minor axis profiles observed in optical passbands on different nights or with a different telescope, with independent determinations of the calibration coefficients. The error estimates are based on the sky noise. Details of the specific observations that were used to determine the difference profiles of Fig. 4 are given in Table 6.

In Fig. 5 a comparison between near-infrared observations obtained on different nights is shown. We notice a significant difference between the individual observations of both ESO 263-G15 and ESO 446-G18 of up to 0.2 mag. This difference is likely due to the slightly varying response of the IRAC2B detector as a function of position across the array. The accuracy of the final, combined K' images is within the observational zero-point uncertainties, however.

The difference minor axis profiles in Figs. 4 and 5 show that in general the internal consistency is well within the zero-point and sky errors; the latter ones being generally of order 0.1–0.2 mag. In some cases differences in seeing show up in the central parts of the minor axis profiles as pronounced features in the difference profiles. We conclude that, although our observations are internally consistent, care has to be taken when interpreting the light at large distances from the galaxy planes, since at those distances the difference between individual observations can amount up to a few tenths of a magnitude. In a few cases, like for ESO 315-G20 and ESO 435-G14, the errors are large due to the low signal-to-noise ratio in either of the minor axis profiles used.

Table 6. Details of the observations used for the internal consistency check of Fig. 4.
Columns: (1) Panel of Fig. 4; (2) Galaxy name (ESO-LV); (3) Passband; (4) and (5) Telescope used (Dan = Danish 1.54m; Dut = Dutch 0.92m) and date of observation (ddmmyy)

Figure	Galaxy (ESO)	Band	Telescope/date (Profile 1)	(Profile 2)
(1)	(2)	(3)	(4)	(5)
(a)	235-G53	*I*	Dan 120794	Dut 170396
(b)	235-G53	*I*	Dut 170396	Dut 210396
(c)	240-G11	*B*	Dut 051094	Dut 061094
(d)	240-G11	*V*	Dut 051094	Dut 061094
(e)	240-G11	*I*	Dut 051094	Dut 061094
(f)	263-G15	*I*	Dan 100194	Dan 110194
(g)	263-G15	*I*	Dan 100194	Dan 130194
(h)	315-G20	*V*	Dut 060194	Dut 090194
(i)	435-G14	*B*	Dut 080493	Dut 201293
(j)	435-G25	*B*	Dut 230493	Dut 231293
(k)	435-G25	*B*	Dut 311293	Dut 050194
(l)	435-G25	*B*	Dut 311293	Dut 060194
(m)	435-G25	*B*	Dut 311293	Dut 230493
(n)	435-G25	*V*	Dut 060194	Dut 231293
(o)	435-G25	*V*	Dut 060194	Dut 221293
(p)	435-G25	*I*	Dut 230493	Dut 231293
(q)	435-G25	*I*	Dut 230493	Dut 060194
(r)	460-G31	*B*	Dan 090794	Dan 110794
(s)	564-G27	*B*	Dut 211293	Dut 221293
(t)	564-G27	*V*	Dut 211293	Dut 221293
(u)	564-G27	*I*	Dut 211293	Dut 221293

3.2 Comparison with published observations

Luminosity profiles of edge-on galaxies observed with modern detectors are scarcely available in the recent literature. For the galaxies in our present sample, a few individual measurements of optical luminosity profiles, either radially, vertically, or azimuthally averaged are available, although they are not sufficiently well documented to prove useful for a detailed comparison to our photometry. Fortunately, however, Mathewson et al. (1992) and Mathewson & Ford (1996), as well as Barteldrees & Dettmar (1993) have published detailed photometry of a significant fraction of our sample galaxies. From the detailed comparison of our photometry to theirs, as discussed in the following sections, our main conclusion is that, within the observational errors, we can reproduce the results published in the literature.

In the near-infrared, detailed surface photometry of edge-on galaxies has been published by Wainscoat et al. (1989) and Aoki et al. (1991), for the large southern edge-on galaxy IC 2531 (ESO 435-G25) and for NGC 891, respectively. The observations of Wainscoat et al. (1989) of IC 2531, a galaxy that we also observed in the near-infrared K' band, were obtained using a raster scan technique with an aperture of $5''$. These scans were made without chopping between galaxy and sky areas, which introduces additional uncertainties due to the rapidly varying sky background in the near-infrared. Although our observations of IC 2531 are of a much higher quality and were taken with a much higher resolution, we find a remarkably good agreement between Wainscoat et al.'s (1989) and

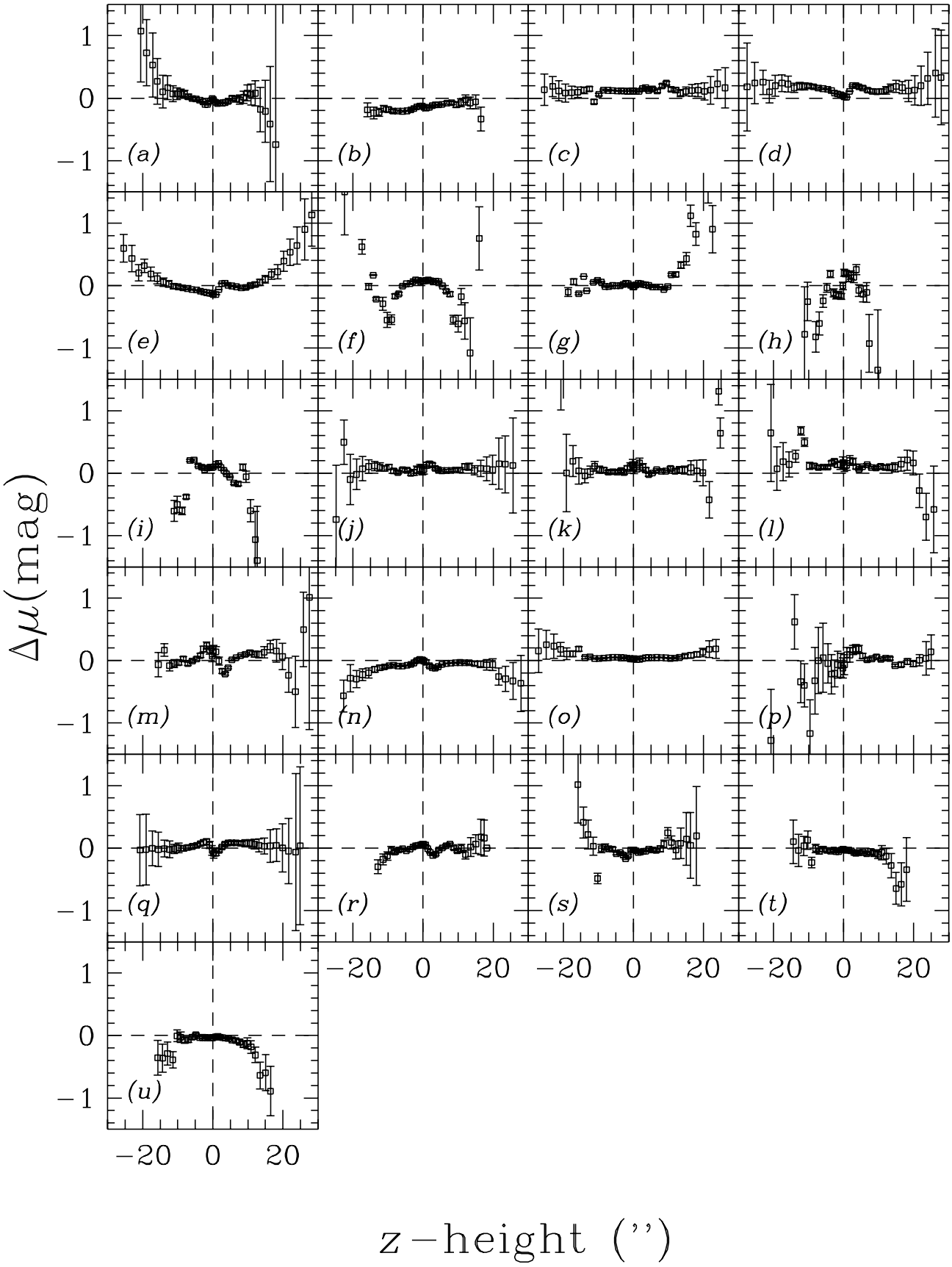

Fig. 4. Comparison of the optical minor axis profiles obtained on different nights or with different telescopes. Details of the observations are given in Table 6

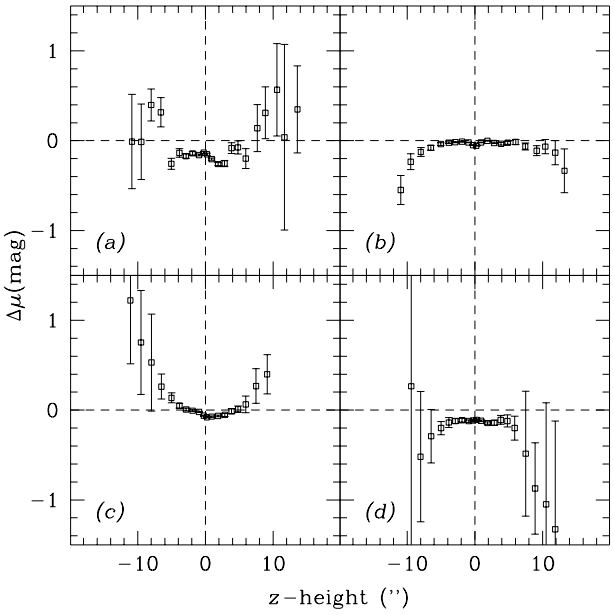

Fig. 5. Comparison of near-infrared minor axis profiles obtained on different nights or with different telescopes. *(a)* K'-band observations of ESO 263-G15, observed on February 24 and 25, 1995; *(b)* and *(c)* Observations of ESO 286-G18 in J and K', observed on July 10 and 11, and on July 9 and 11, 1995, respectively; *(d)* K'-band observations of ESO 446-G18, obtained on July 9 and 12, 1995.

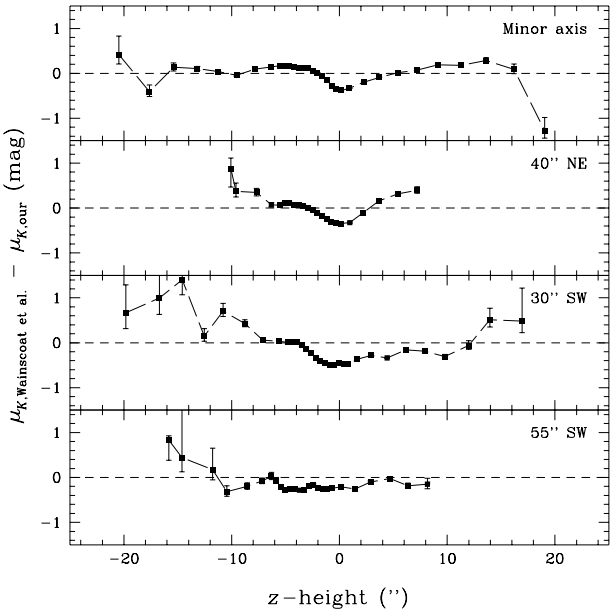

Fig. 6. Comparison of K'-band vertical profiles from Wainscoat et al. (1989) and our observations. To obtain these profiles we averaged strips of 7.″5 wide.

our K'-band observations, as can be seen in Fig. 6. We have extracted vertical profiles from our calibrated K'-band image at exactly the same positions and in the same way as was done by Wainscoat et al. (1989). The distinct drop in the difference profiles at the position of the galaxy plane is caused by the difference in resolution between both data sets.

3.2.1 Comparison with Mathewson et al. (1992)

A large and homogeneous set of observations of southern Sb–Sc galaxies has been published recently by Mathewson et al. (1992) and Mathewson & Ford (1996). They present luminosity profiles in the Kron-Cousins I band, to which system we also calibrated our observations.

Azimuthally averaged luminosity profiles were obtained by fitting ellipses to the galaxy isophotes, whose intensity, ellipticity and position angle were allowed to vary with each ellipse. Bad pixels, cosmic rays and foreground stars were masked out, so that these would not affect the results from the ellipse-fitting routine. Although this method works sufficiently well for low and moderately-inclined galaxies, when dealing with highly-inclined or edge-on galaxies the ellipse fitting is severely influenced by the presence of a central dust lane and the non-elliptical outer galaxy isophotes. Unfortunately, since Mathewson et al. (1922) and Mathewson & Ford (1996) did not tabulate the ellipticities nor the position angles used for the individual ellipses obtained for each galaxy, we can at best compare azimuthally averaged profiles which were obtained with the same free parameters. A comparison between the azimuthally averaged I-band luminosity profiles of Mathewson et al. (1992) and Mathewson & Ford (1996) and those obtained from our observations is shown in Fig. 7.

In general, we find that the differences between our and Mathewson's measurements are small, although clear deviations are appreciated in a number of cases. In particular for those galaxies for which the difference between our and Mathewson's profiles is relatively large (e.g., ESO 138-G14), we used the individual observations to check our results. It was found that the features shown in Fig. 7 can be reproduced to within the observational errors. The main cause of deviations between Mathewson's and our profiles, in particular at small semi-major axis radii, is the unpredictable influence of dust, which significantly affects the ellipse fitting in the inner galaxy regions.

3.2.2 Comparison with Barteldrees & Dettmar (1993)

Barteldrees & Dettmar (1993) presented detailed optical surface photometry for a sample of 27 edge-on disk galaxies, which has 8 galaxies in common with our sample. The observations were done in the Thuan & Gunn (1976) g and r bands, for which the transformation to the Johnson B band is obtained as follows (Barteldrees & Dettmar, 1993; Thuan & Gunn, 1976):

$$g = B - 0.423(B - R) - 0.14 \quad (3)$$

and

$$r = B - 1.78(B - V) + 0.37 \quad (4)$$

We extracted surface brightness profiles along the galaxies' major axes, and compared these to the major axis profiles plotted by Barteldrees & Dettmar (1993). To do so, we calculated the transformations from the standard Johnson B band to Thuan & Gunn (1976) g and r band, using B–V and B–R

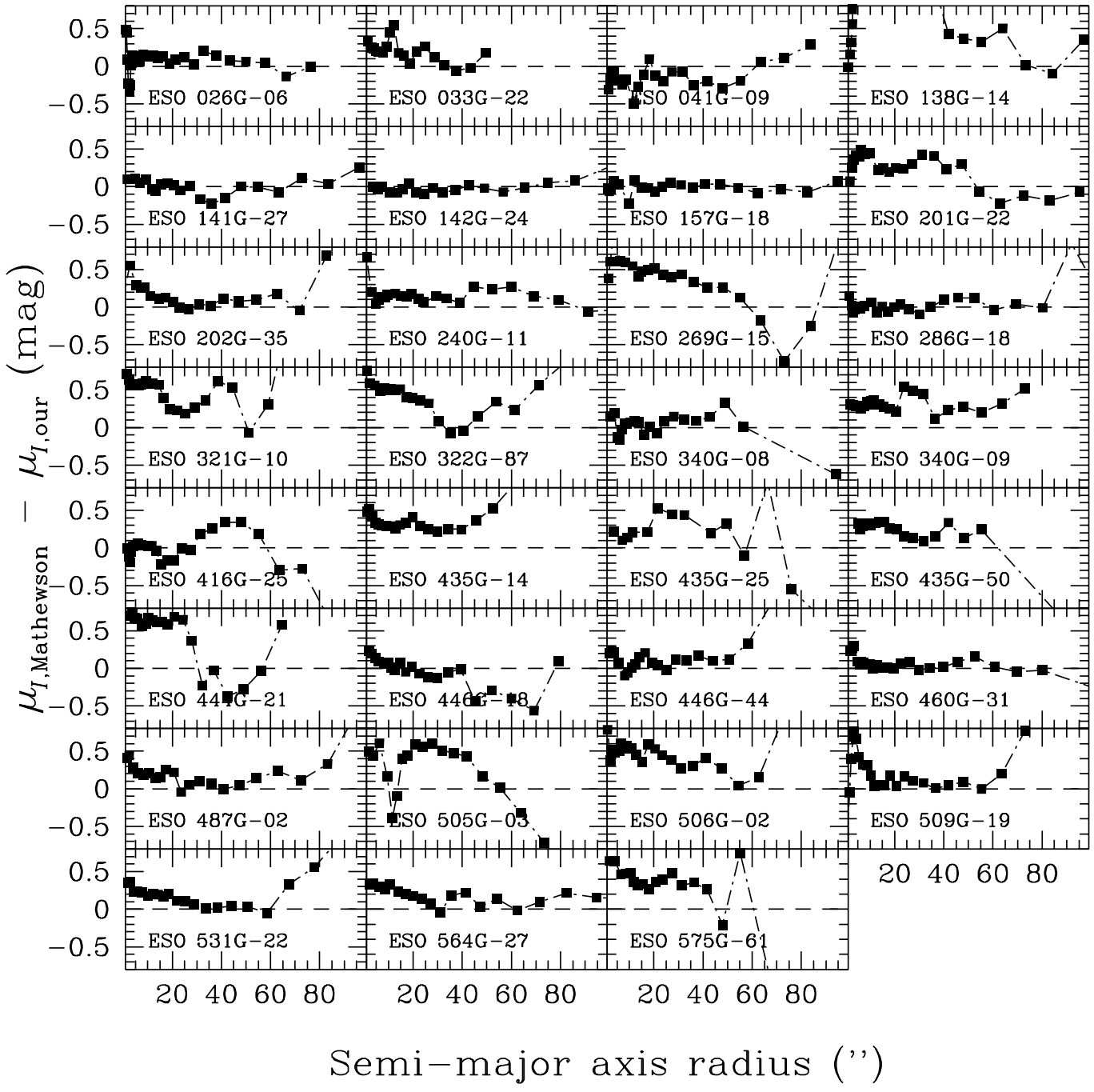

Fig. 7. Comparison between azimuthally averaged I-band profiles published by Mathewson et al. (1992) and Mathewson & Ford (1996), and those obtained from fitting ellipses to our observations.

colours taken from the ESO-LV or determined independently from our own observational data. The resulting difference profiles are shown in Fig. 8. The close agreement resulting from this comparison leads us to the conclusion that our photometry reproduces that of Barteldrees & Dettmar (1993) to within the observational uncertainties.

4 Summary and Conclusions

In this Chapter I have described the selection criteria that were applied to both the UGC and the ESO-LV catalogues to yield statistically complete samples in both the northern and the southern hemispheres. The final samples, from which random subsamples were observed, are statistically complete for edge-on disk galaxies with a limiting blue major axis diameter of $2.'2$, which can easily be corrected to represent a volume-

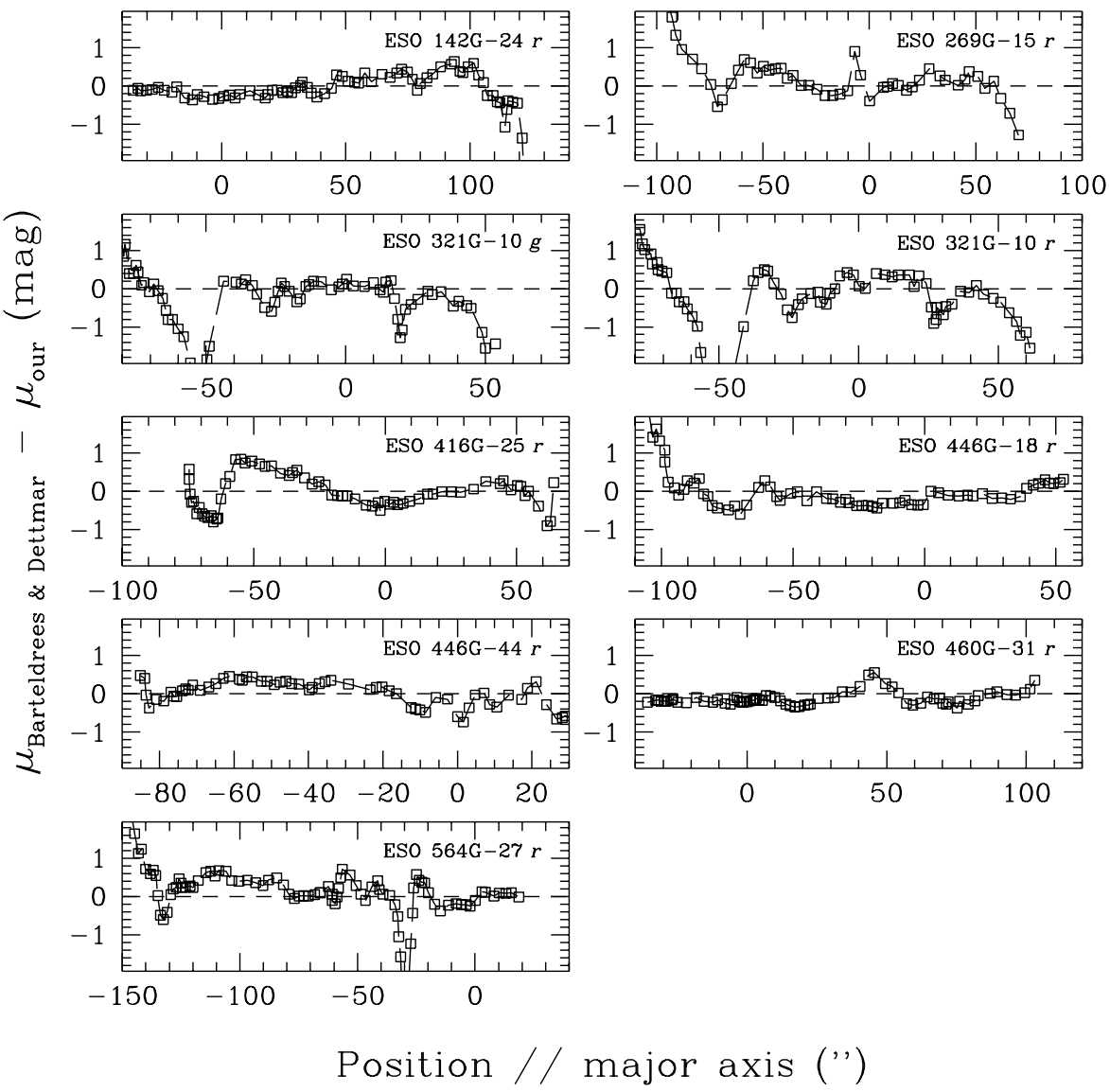

Fig. 8. Comparison between major axis r (and g)-band profiles published by Barteldrees & Dettmar (1993), and those extracted from our observations. The width of our major axis profiles was chosen to be in the order of the seeing FWHM, since Barteldrees & Dettmar (1993) did not specify this.

limited sample. For the southern sample, our observed subsample proves to be statistically complete, based on a $V/V_{\rm max}$ test. Therefore, the results obtained in this Ph.D. Thesis can be considered to be statistically significant for "normal" disk galaxies.

The observations and reduction procedure have been described in detail. The observations prove to be consistent, both when comparing individual observations obtained on different nights or with a different telescope, and when compared to luminosity profiles previously published in the literature. The observations and photometry presented in this Ph.D. Thesis are accurate to within the observational zero-point uncertainties.

Acknowledgements – I would like to thank the following observers at the Dutch 92cm telescope at La Silla, Chile, who have provided me with additional observations needed for this statistical study: Harro Verkouter (Kapteyn Astronomical Institute, Groningen, April 1993), Jos de Bruijne (Sterrewacht Leiden, December 1993/January 1994), Peter van Dokkum (Kapteyn Astronomical Institute, Groningen, September/October 1994), Jeroen de Jong (Sterrenkundig Instituut "Anton Pannekoek", Amsterdam, January 1995), and Ciska Kemper (Sterrewacht Leiden, March 1996). Reynier Peletier assisted me when observing in the near-infrared with the ESO/MPI 2.2m telescope in July 1994. Furthermore, acknowledgements are due to Piet van der Kruit, Reynier Peletier, Roelof de Jong, Rob Swaters and Rolf Jansen for

their input in the sample selection and the calibration of the observations.

References

Aoki, T.E., Hiromoto, N., Takami, H., Okamura, S., 1991, PASJ 43, 755

Barteldrees, A., Dettmar, R.-J., 1993, A&AS 103, 475

Bessel, M.S., 1990, PASP 102, 1181

Bothun, G.D., Gregg, M.D., 1990, ApJ 350, 73

Bottinelli, L., Durand, N., Fouqué, P., Garnier, R., Gouguenheim, L., Loulergue, M., Paturel, G., Petit, C., Teerikorpi, P., 1993, A&AS 102, 57

Bottinelli, L., Gouguenheim, L., Fouqué, P., Paturel, G., 1990, A&AS 82, 391

Buser, R., 1978, A&A 62, 411

Carter, B.S., Meadows, V.S., 1995, MNRAS 276, 734

Da Costa, L.N., Pellegrini, P.S., Nunes, M.A., Willmer, C., Latham, D.W., 1984, AJ 89, 1310

Da Costa, L.N., Nunes, M.A., Pellegrini, P.S., Willmer, C., Chincarini, G., Cowan, J.J., 1986, AJ 91, 6

Da Costa, L.N., Pellegrini, P.S., Willmer, C., De Carvalho, R., Maia, M., Latham, D.W., Geary, J.C., 1989, AJ 97, 315

Davies, J.I., 1990, MNRAS 244, 8

de Grijs, R., Peletier, R.F., van der Kruit, P.C., 1997, A&A, in press **(Chapter 8)**

de Grijs, R., van der Kruit, P.C., 1996, A&AS 117, 19 **(Chapter 4)**

de Jong, R.S., 1994, A&AS 106, 451

de Vaucouleurs, G., de Vaucouleurs, A., Corwin, H.G., Buta, R.J., Paturel, G., Fouqué, P., 1991, Third Reference Catalog of Bright Galaxies, New York: Springer (RC3)

Dressler, A., 1991, ApJS 75, 241

Fairall, A.P., Willmer, C.M.A., Calderon, J.H., Latham, D.W., Da Costa, L.N., Pellegrini, P.S., Nunes, M.A., Focardi, P., Vettolani, G., 1992, AJ 103, 11

Fisher, F.B., Huchra, J.P., Strauss, M.A., Davis, M., Yahil, A., Schlegel, D., 1995, ApJS 100, 69

Han, M., 1992, ApJS 81, 35

Huizinga, J.E., 1994, Ph.D. Thesis, University of Groningen

Karachentsev, I., 1989, AJ 97, 1566

Knapp, G.R., Guhathakurta, P., Kim, D.-W., Jura, M., 1989, ApJS 70, 329

Landolt, A.U., 1992a, AJ 104, 340

Landolt, A.U., 1992b, AJ 104, 372

Lauberts A., Valentijn, E.A., 1989, The Surface Photometry Catalogue of the ESO-Uppsala Galaxies, ESO **(ESO-LV)**

Mathewson, D.S., Ford, V.L., Buchhorn, M., 1992, ApJS 81, 413

Mathewson, D.S., Ford, V.L., 1996, ApJS 107, 97 (AAS CD-ROM Series, Vol. 7)

Nilson, P., 1973, Uppsala General Catalogue of Galaxies **(UGC)**, Uppsala

Peletier, R.F., 1993, A&A 271, 51

RGO/La Palma Technical Notes 37, 1987 (Isaac Newton Group, La Palma)

RGO/La Palma Technical Notes 73, 1990 (Isaac Newton Group, La Palma)

Roberts, M.S., Hogg, D.E., Bregman, J.N., Forman, W.E., Jones, C., 1991, ApJS 75, 751

Schmidt, K.-H., Boller, T., 1992, Astron. Nachr. 313, 189

Schmidt, M., 1968, ApJ 151, 393

Schommer, R.A., Bothun, G.D., Williams, T.B., Mould, J.R., 1993, AJ 105, 97

Thuan, T.X., Gunn, J.E., 1976, PASP 88, 543

Thuan, T.X., Seitzer, P.O., 1979, ApJ 231, 680

van der Kruit, P.C., Searle, L.S., 1981, A&A 95, 105

Wainscoat, R.J., Freeman, K.C., Hyland, A.R., 1989, ApJ 337, 163

Wainscoat, R.J., Cowie, L.L., 1992, AJ 103, 332